Mechanism of nanocrystalline microstructure formation in amorphous Fe-Nb-B alloys

Akihiko Hirata,[1,*] Yoshihiko Hirotsu,[1] Eiichiro Matsubara,[2] Tadakatsu Ohkubo,[3] and Kazuhiro Hono[3]
[1]*Institute of Scientific and Industrial Research, Osaka University, Ibaraki, Osaka 567-0047, Japan*
[2]*Department of Materials Science and Engineering, Kyoto University, Sakyo, Kyoto 606-8501, Japan*
[3]*National Institute for Materials Science, 1-2-1 Sengen, Tsukuba 305-0047, Japan*
(Received 24 May 2006; revised manuscript received 21 August 2006; published 15 November 2006)

To understand the mechanism of the high number density of bcc-Fe nanocrystals in a partially crystallized $Fe_{84}Nb_7B_9$ alloy, we have investigated detailed local structural and compositional changes on annealing amorphous ribbons using transmission electron microscopy, three-dimensional atom probe, and high-energy x-ray diffraction techniques. Nanobeam electron diffraction patterns from an as-quenched amorphous ribbon indicated a local nanoscale atomic ordering. On annealing, reduced interference functions showed a clear change just below the crystallization temperature (~773 K). At this stage, local compositional fluctuations started to appear, and medium-range ordering with a bcc-Fe structure as small as 2 nm was clearly observed in high-resolution electron micrographs with an extremely high number density. Pair distribution function analyses suggested a structural change at this stage of annealing to increase the chemical bonds in the residual amorphous matrix around the bcc-Fe regions. The increase of atomic chemical bonds in the residual amorphous matrix is considered to retard the growth of the bcc-Fe nanocrystals after the coalescence of bcc-Fe MRO regions in the later stage of annealing. These results suggest that bcc-Fe nanocrystallization with the extremely high number density is ascribed to primarily (i) the presence of highly dense bcc-Fe MRO regions and (ii) the increase of chemical bonds of matrix atoms on annealing.

DOI: 10.1103/PhysRevB.74.184204 PACS number(s): 81.05.Kf, 61.14.Lj, 61.43.Dq, 61.50.Ks

I. INTRODUCTION

Crystallization in amorphous alloys with a large number density of nanocrystals has attracted much attention because of their applications to nanocrystalline soft magnetic materials and nanocomposite hard magnetic materials.[1] Despite many previous investigations,[2] the mechanism of nanocrystallization in amorphous alloys with a high number density of nucleation has not been thoroughly understood. According to the classical nucleation theory, the number density of nuclei in the primary crystallization of amorphous alloys is estimated to be less than 10^{19} m^{-3}, thus the classical nucleation theory cannot be used to explain the appearance of nanocrystals with extremely high number density (10^{23}–10^{24} m^{-3}).[3,4] The following models have been proposed to explain such high-density nanocrystallization: a model of composition fluctuation in the amorphous state prior to crystallization,[5–7] a heterogeneous nucleation model that posits a high density of impurities or insoluble constituent nucleation sites,[8,9] and a homogeneous nucleation model with little or no activation energy.[4] These alternative nanocrystallization mechanisms are now under examination mainly for crystallizations in various amorphous alloy systems.

In Fe-based amorphous alloys, the formation of bcc-Fe nanocrystals is important for applications as nanocrystalline soft magnetic materials. For the $Fe_{73.5}Si_{13.5}B_9Nb_3Cu_1$ alloy, which is well known as FINEMET,[10] detailed analyses have been employed for elucidating the origin of the bcc-Fe nanocrystallization with a particle size of about 10 nm.[8,11] In this system, insoluble Cu clustering occurs prior to the primary crystallization stage of bcc-Fe, and the fcc-Cu particles that evolve from the clusters are considered to become heterogeneous nucleation sites for the high-density bcc-Fe nanocrystals during annealing. The role of the fcc-Cu particles in nanocrystallization has also been confirmed in a $Fe_{89}Zr_7B_3Cu_1$ alloy, in which a bcc-Fe nanocrystal was directly observed in direct contact with fcc-Cu by high-resolution electron microscopy (HREM).[12]

However, the dense formation of bcc-Fe nanocrystals with an extremely high number density has also been found even in Cu-free Fe-*M*-B (*M*=Nb, Zr, Hf) alloy systems,[13] although their Cu-added alloys exhibit a higher number density of precipitates than those without Cu. The mechanism of nanocrystallization in the Cu-free alloys, where the number density is comparable to those of the Cu-added alloys, remains an open question. In this paper, we demonstrate detailed structural and compositional analyses in the nanocrystallization process of an amorphous $Fe_{84}Nb_7B_9$ alloy by means of three different complementary methods, i.e., transmission electron microscopy (TEM) with accelerating voltages of 200 and 300 kV, three-dimensional atom probe (3DAP), and high-energy x-ray diffraction using synchrotron radiation. The TEM technique enables us to obtain nanoscale local structural information, whereas the x-ray diffraction presents precise averaged structure information taken from an extended region through a pair distribution function analysis. In addition, 3DAP has been used to investigate the local chemical information with a near-atomic resolution. Therefore, this complementary study can provide a comprehensive understanding for the mechanism of nanocrystallization with the extremely high number density.

II. EXPERIMENTAL PROCEDURE

An amorphous $Fe_{84}Nb_7B_9$ ribbon with a thickness of about 20 μm was prepared by the single-roll melt spinning method. The samples were continuously heated to various

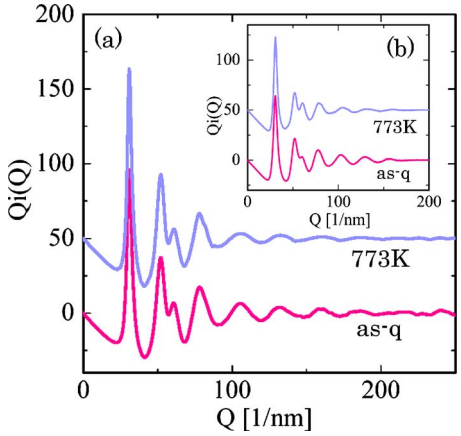

FIG. 1. (Color online) Reduced interference functions of as-quenched and annealed (773 K) specimens obtained by (a) high-energy x-ray diffraction and (b) energy-filtered electron diffraction techniques.

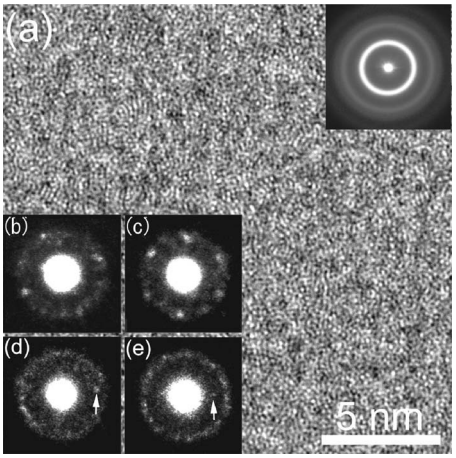

FIG. 2. (a) HREM image and (b)–(e) NBED patterns taken from an as-quenched specimen.

temperatures in a differential scanning calorimetry furnace with a heating rate of 20 K/min. For transmission electron microscopy study, the specimens were thinned by Ar-beam thinning under a low beam angle ($<10°$) with a low voltage (<2 kV) and also by electropolishing with an electrolyte of 6 vol. % perchloric acid in acetic acid. Note that these different sample preparation techniques basically did not result in any difference in the HREM and electron diffraction. Energy-filtered diffraction patterns were obtained using a LEO-922D (200 kV). Nanobeam electron-diffraction (NBED) patterns and HREM images were taken using a JEM-3000F (300 kV) TEM. The TEM images and SAED patterns were recorded on imaging plates (IP) and read using IP readers (DITABIS-MICRON and FDL-5000). The NBED patterns were recorded by a TV-rate CCD camera. High-energy x-ray diffraction was measured at BL-04B2 in SPring-8, Harima, Japan. To reduce the truncation errors in the Fourier transform, the x-ray intensity profile was taken up to a high-scattering wave vector of $Q_{max}=250$ nm^{-1}. The detailed procedure has already been described in a previous paper.[14] The 3D chemical mapping was performed by a locally built energy compensated 3DAP equipped with the Oxford Nanoscience delay line detector. Needlelike specimens for atom probe analysis were prepared by electropolishing square rods of approximately 20 μm$\times$20 μm$\times$5 mm, which were prepared from the ribbon by mechanical grinding.[2]

III. RESULTS AND DISCUSSION

First we examined the structural change on annealing prior to nanocrystallization. From a previous study,[14] the initial crystallization is known to start at around 773 K. Figure 1 shows a series of reduced interference functions [Qi(Q)] taken from a specimen annealed up to 773 K, together with the as-quenched specimen, where Q is the scattering vector ($4\pi \sin\theta/\lambda$: θ is the scattering angle and λ is the x-ray or electron wavelength) and $i(Q)$ is the interference function. The profiles shown in Fig. 1(a) were taken using the high-energy x-ray diffraction technique, and those in Fig. 1(b) were obtained from energy-filtered selected area electron diffraction (SAED) patterns (200 kV TEM). The characteristics of the change in Qi(Q) for both x-ray and electron diffraction on annealing are almost the same as shown in the figures, indicating that the fundamental structural feature is independent of the analysis areas of the specimen. In comparison with the case of the as-quenched specimen, larger relative heights of the first and second peaks and faster dumping of oscillations of Qi(Q) are found for the annealed specimen. This indicates that the amorphous structure changes during the annealing prior to the nanocrystallization. This will be discussed later in detail.

Next we examined the microstructures of both specimens using TEM to clarify the microscopic feature of the structural change. An HREM image and NBED patterns taken from the as-quenched specimen are shown in Fig. 2(a) and Figs. 2(b)–2(e), respectively (300 kV TEM). The corresponding SAED pattern obtained from the same region is also shown in the inset in Fig. 2(a). The SAED pattern shows halo rings due to the fully amorphous state. The HREM image of Fig. 2(a) was taken under the optimum defocus condition (60 nm underfocus) suitable for detecting local lattices with interplanar spacings ranging from 0.25 to 0.18 nm in high contrast.[15] No clear local lattice fringe images are observed in Fig. 2(a). In our previous studies on amorphous $Fe_{84}B_{16}$ and $Fe_{90}Zr_7B_3$ alloys,[16,17] local regions with bcc-like structure were observed as crossed lattice fringe regions as small as 1 nm. These small local regions that exhibit lattice fringe images may be called atomic medium range order (MRO) in the sense of amorphous local structures. Although MRO regions with the bcc-Fe type structure were not observed clearly with HREM in this specimen, clear diffraction spots were detected in NBED patterns. In Figs. 2(b) and 2(c), diffraction spots with fourfold and sixfold symmetries are observed by NBED with a beam size of about 1.5 nm. From additional information that the reciprocals of these diffraction vectors are all close to 0.20 nm, the diffraction patterns in Figs. 2(b) and 2(c) were found to correspond to those of the bcc-Fe structure with $\langle 100\rangle$ and $\langle 111\rangle$ beam incidences, respectively. This result is consistent with the previous high-

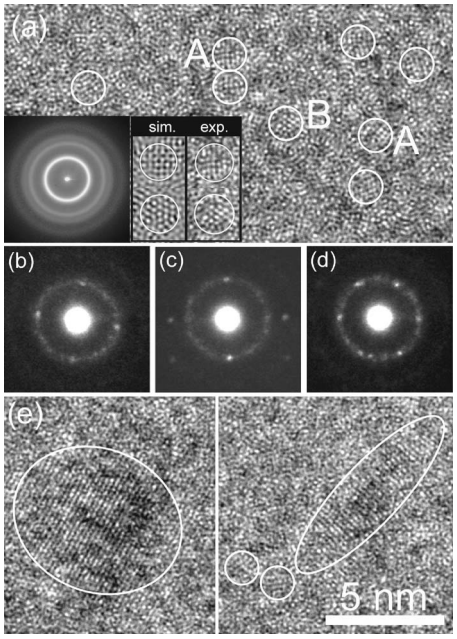

FIG. 3. (a) HREM image taken from an annealed specimen (773 K), together with NBED patterns in (b), (c), and (d). Simulated HREM image is also shown in the inset of (a). (e) HREM image of minor regions in the specimen annealed up to 773 K.

energy x-ray diffraction analysis indicating the existence of the bcc-type structural ordering in the as-quenched state.[14] On the other hand, the diffraction spots indicated by arrows in Figs. 2(d) and 2(e) are presumably due to the compound structures, according to the corresponding interplanar spacings of about 0.30 and 0.24 nm, respectively. Hence, the NBED technique revealed the existence of a very fine scale structural ordering directly as reported in our previous studies,[16–18] although such a fine scale structural feature could not be clearly imaged by HREM.

Figure 3(a) shows a typical HREM image obtained from the specimen annealed at 773 K (300 kV TEM). The image was also taken under the 60 nm underfocus condition. A SAED pattern from the area is shown in the inset. In this stage, bcc-Fe MRO (local lattice fringe regions) with sizes of about 1–1.5 nm are clearly observed with a very high density in the HREM image. The fringe spacings and their cross angles of these images are consistent with those from the bcc-Fe structure. For example, encircled clear bcc-Fe MRO indicated as *A* and *B* correspond to the bcc-Fe MRO with the ⟨100⟩ and ⟨111⟩ orientations, respectively. An HREM image simulation was performed to confirm that the images observed in regions *A* and *B* are those of bcc-Fe MRO. The structural model for the simulation consisted of 10 000 atoms in a tetragonal cell with a size of $3.87 \times 3.87 \times 7.75$ nm^3 and included two ⟨111⟩ and ⟨100⟩ oriented bcc-Fe clusters with a diameter of 2 nm embedded in an amorphous matrix with dense-randomly packed Fe, Nb, and B atoms. A physical density of the model was set to be 7.77 g/m^3, which is identical to that of the as-quenched specimen determined by the Archimedean method. Nb and B atoms are also included in the bcc-Fe MRO. The ⟨100⟩ and ⟨111⟩ bcc-Fe MRO images simulated under the defocus of 60 nm reproduce the experimental local images at *A* and *B*. Although the bcc-Fe MRO in the model are 2 nm in size, apparent MRO regions in the simulated images were as small as 1.5 nm. This is because a clear imaging of the bcc-Fe MRO is disturbed by the amorphous matrix structure overlapped along the beam direction. In addition to the HREM image, we confirmed the existence of the bcc-Fe MRO directly by using the NBED technique. The NBED patterns obtained from various regions in Fig. 3(a) are shown in Figs. 3(b)–3(d), which correspond to the ⟨100⟩, ⟨110⟩, and ⟨111⟩ zones, respectively. This indicates that the bcc-Fe MRO regions grow on annealing in the amorphous matrix. In addition, we occasionally found clear bcc-Fe nanocrystals grown as large as 3–10 nm as shown in Fig. 3(e). The SAED patterns from the areas including such regions showed weak diffraction spots identified as those from bcc-Fe (not shown). The contribution of the nanocrystals to the whole diffraction intensity is, however, negligible because of their small volume faction. Thus, the reflections from them hardly contribute to the interference functions in the x-ray diffraction structure analysis at this annealing stage.

A 3DAP elemental analysis was made for the as-quenched and annealed (~773 K) specimens to examine the change of the nanoscale compositional fluctuation during annealing. Since there was no obvious compositional fluctuation in both of the 3D elemental maps, we examined the deviation of the frequency distribution of compositions from the binomial distribution, which can be regarded as random compositional distribution, using the χ^2 test. Note that the binomial distribution is determined by a composition, a number of the atoms in one block, and a number of blocks. Figure 4 shows the frequency distributions of Fe, Nb, and B concentrations analyzed for more than 3000 blocks (one block consists of 100 atoms) obtained by 3DAP. The histograms show the experimental results, whereas the solid curves are the binomial distribution functions for random distribution. The frequency distribution of the homogeneous state should follow the binomial distribution. For each element, the χ^2 value, the degree of freedom (ν), and the significance probability value (P value) are written in the figures.[19] In the as-quenched specimen, the P values are relatively large, indicating that the compositional fluctuation is negligible, that is, a homogeneous compositional distribution. On the other hand, the small P values of the specimen annealed up to 773 K indicate that an appreciable compositional fluctuation occurs at the stage of 773 K. Thus, the 3DAP analyses reveal that the local compositional fluctuation starts to occur after annealing at about 773 K concurrently with the structural change observed in Fig. 3.

Since we found the clear high-density bcc-Fe MRO regions by HREM and the local compositional fluctuation by 3DAP in the annealed state, the amorphous matrix phase should have changed both structurally and chemically in the course of annealing. Here, we focus on the change of the atomic correlations especially in the amorphous matrix except for the bcc-Fe MRO regions. The total pair distribution functions (PDF) were obtained from the Fourier transform of the x-ray reduced interference functions in Fig. 1(a). Figure 5 shows the first peaks of PDFs from the as-quenched and annealed (up to 773 K) specimens. Note that the first PDF

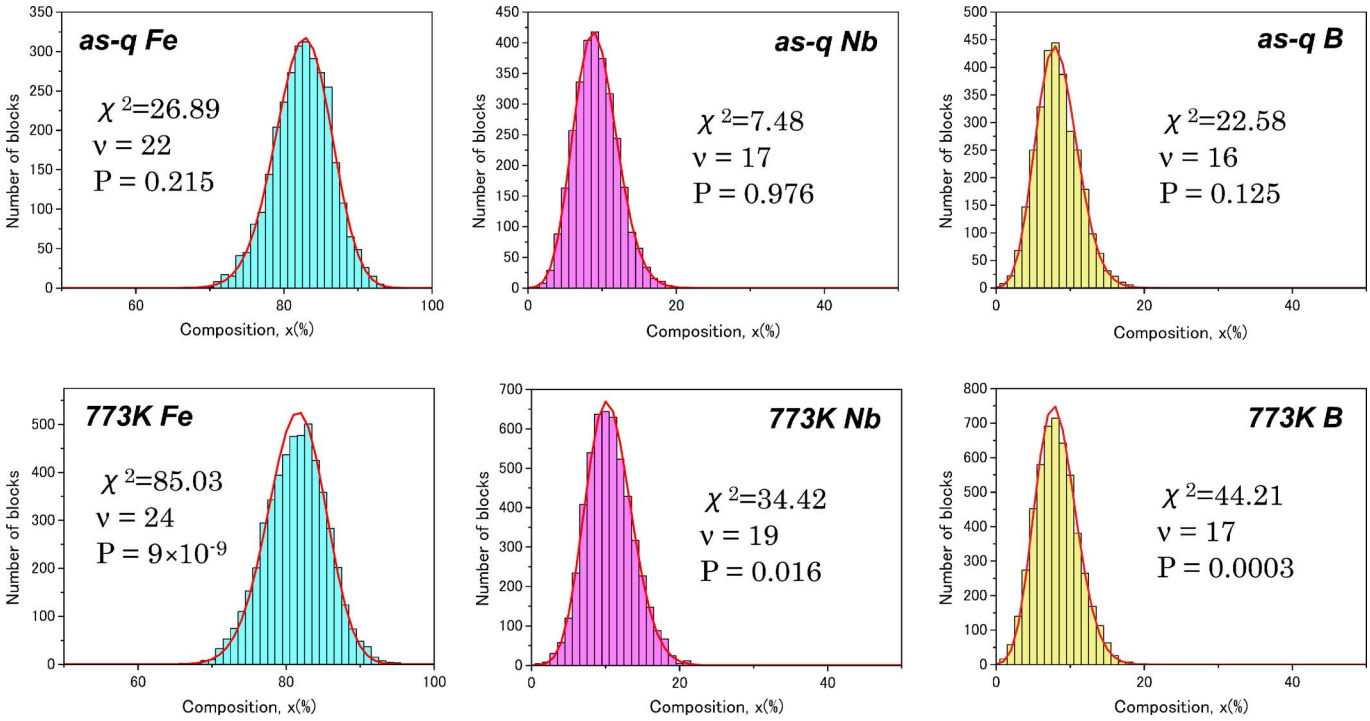

FIG. 4. (Color online) Frequency distribution diagrams of 3D elemental mapping for each element obtained from (a) as-quenched and (b) annealed (773 K) specimens.

peak profiles in Fig. 5 give us precise atomic near-neighbor correlation as a result of the scattering information up to high Q ($Q \sim 250$ nm^{-1}). The Fe-Fe distances for bcc-Fe structure are indicated by arrows. The first PDF peak of the annealed specimen has the maximum at a slightly larger radial distance compared with that for the as-quenched specimen, and also has an increase of $g(r)$ in the shorter radial distance range. Such an increase of $g(r)$ at smaller r values can only be explained by assuming shorter Fe-Fe bond distances in the annealed structure shorter than that for bcc Fe. Note that the change is considered to arise from a residual amorphous matrix surrounding the bcc-Fe nanophases. The shorter atomic correlation is probably related to the local development of local chemical order in the matrix. Since the amorphous phase was found to decompose into bcc-Fe and α-Mn-type compound phases at higher temperature,[20] it is well presumed that the development of local chemical order in the matrix is closely related to a formation of local α-Mn-like cluster structures in fine scale, which cannot be observed by HREM. Note that the short Fe-Fe atomic distances are found in the α-Mn-type compound structure.

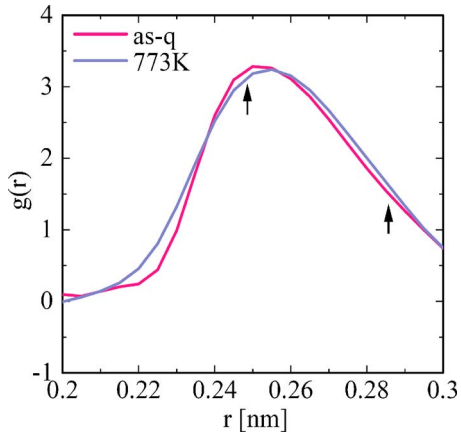

FIG. 5. (Color online) Pair distribution functions of (a) as-quenched and (b) annealed (773 K) specimens obtained by the high-energy x-ray diffraction technique.

Schroers *et al.* reported that the high number density of nucleation (10^{23}–10^{24} m^{-3}) cannot be explained by the classical nucleation theory,[3] in which even the highest nucleation density is less than 10^{19} m^{-3}. In the case of Zr-based bulk metallic glasses, spinodal decomposition in the amorphous state (amorphous phase separation) with a large compositional fluctuation prior to nanocrystallization has been proposed to explain the nanocrystallization.[5–7] However, according to the modern nucleation theory where a diffuse interface is considered,[4] the energy barrier to the crystal nucleation can diminish or disappear at a high supercooling and can provide the high-density nucleation. They also mentioned that the high-density nucleation cannot be explained within a framework of the classical nucleation theory, even if the spinodal decomposition is taken into account. In the present system, no long-range compositional fluctuation expected from a spinodal decomposition was observed prior to nanocrystallization. There have also been some recent reports in several alloy systems that no amorphous phase separation was observed before the nanocrystallization.[21–24] Under this situation, a continuous development of the quenched-in local structural ordering on annealing, as represented in this study, is rather consistent with the modern nucleation theory. The quenched-in local structural ordering is considered to origi-

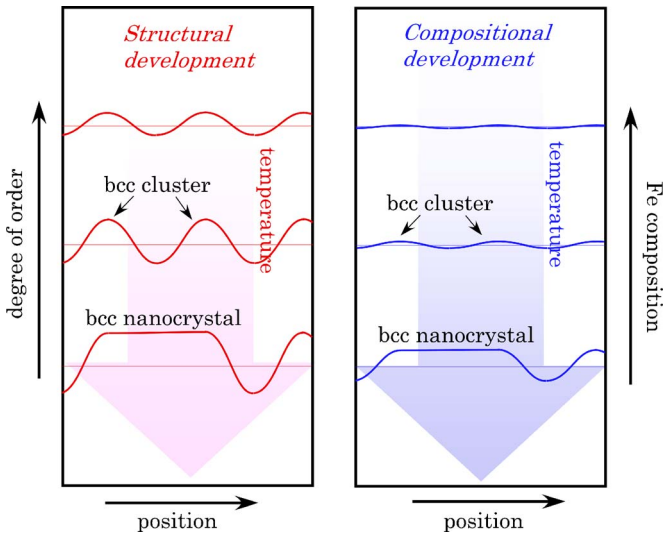

FIG. 6. (Color online) Schematic diagram of structural and compositional changes in the present nanocrystallization model.

nate from local atomic movements during the rapid quenching. It is likely that the local structural ordering triggers high-density bcc-Fe MRO, giving rise to nanocrystallization during annealing. Since a number density of the observed local bcc-Fe MRO regions was estimated to be more than 10^{25} m^{-3}, which is much higher than that of the nanocrystals after crystallization (10^{23}–10^{24} m^{-3}), their growth and coalescence would generate the resultant bcc-Fe nanocrystals with grain sizes of about 10 nm. The anisotropic shape of the growing bcc-Fe grain shown in Fig. 3(e) also supports the coalescence growth mechanism, because the bcc-Fe crystal structure has a cubic symmetry. Based on the above results, the structural and compositional changes in the present nanocrystallization model are conceptually depicted with three steps in Fig. 6. First, as shown by the NBED and 3DAP results, structural ordering occurs locally even in the as-quenched state with a negligible compositional fluctuation. In the next annealing stage (annealed up to 773 K), the structural ordering with the bcc-Fe structure develops with a gradual local compositional change, as observed in NBED, HREM, and 3DAP. At this stage, the structural change in the matrix, which is probably due to an increase of the chemical bonding, was detected in the residual amorphous matrix by x-ray-diffraction analysis. The bcc-Fe nanophases eventually combine into the large bcc-Fe nanocrystals in the final stage. At this stage, Fe-atom diffusion is considered to be retarded due to the increase of chemical bonds in the matrix, which inhibits the overgrowth of the bcc-Fe nanocrystals giving a high number density of the nanocrystals. Even in this stage, some amount of B atom presumably remains in the bcc-Fe nanocrystals.[25]

IV. CONCLUSIONS

In the $Fe_{84}Nb_7B_9$ alloy, the amorphous phase is found to contain a high number density of bcc MRO regions prior to nanocrystallization. The local structural ordering (the MRO formation) exists without any compositional fluctuation in the as-quenched state. On annealing, the nanoscale structural ordering developed with the detectable compositional change and is not equivalent to the amorphous phase separation, as was reported mainly in the Zr-based system. The experimental results seem to be reasonable within a framework of the modern nucleation theory, where a nucleation barrier diminishes at a large supercooling, that is, the growth mode becomes dominant. In addition, the grain growth is inhibited by an enhancement of the chemical bond in the residual amorphous matrix to retard the Fe-atom diffusion.

ACKNOWLEDGMENTS

This paper was supported partly by a Grant in Aid from the Ministry of Education, Sports, Culture, Science and Technology, Priority Area on "Materials Science of Bulk Metallic Glasses." We thank A. Makino for supplying the samples. One of us (A.H.) also acknowledges A. Koreeda for his technical assistance. E.M. thanks the staff of the SPring-8, especially S. Kohara and H. Ohsumi, for their kind help in the high-energy diffraction measurements.

*Author to whom correspondence should be addressed. Electronic address: ahirata@sanken.osaka-u.ac.jp

[1] T. Kulik, J. Non-Cryst. Solids **287**, 145 (2001).
[2] K. Hono, Prog. Mater. Sci. **47**, 621 (2002).
[3] J. Schroers, R. Busch, A. Masuhr, and W. L. Johnson, Appl. Phys. Lett. **74**, 2806 (1999).
[4] H. Assadi and J. Schroersb, Acta Mater. **50**, 89 (2002).
[5] S. Schneider, P. Thiyagarajan, and W. L. Johnson, Appl. Phys. Lett. **68**, 493 (1996).
[6] J. F. Loffler and W. L. Johnson, Appl. Phys. Lett. **76**, 3394 (2000).
[7] X.-L. Wang, J. Almer, C. T. Liu, Y. D. Wang, J. K. Zhao, A. D. Stoica, D. R. Haeffner, and W. H. Wang, Phys. Rev. Lett. **91**, 265501 (2003).
[8] K. Hono, D. H. Ping, M. Ohnuma, and H. Onodera, Acta Mater. **47**, 997 (1999).
[9] C. T. Liu, M. F. Chisholm, and M. K. Miller, Intermetallics **10**, 1105 (2002).
[10] Y. Yoshizawa, S. Oguma, and K. Yamauchi, J. Appl. Phys. **64**, 6044 (1988).
[11] K. Hono, K. Hiraga, Q. Wang, A. Inoue, and T. Sakurai, Acta Metall. Mater. **40**, 2137 (1992).
[12] T. Ohkubo, H. Kai, D. H. Ping, K. Hono, and Y. Hirotsu, Scr. Mater. **44**, 971 (2001).
[13] A. Makino, A. Inoue, and T. Masumoto, Mater. Trans., JIM **36**, 924 (1995).
[14] E. Matsubara, S. Tanaka, A. Makino, and T.-H. Chiang, Mater. Trans., JIM **45**, 1199 (2004).
[15] Y. Hirotsu, T. Ohkubo, and M. Matsushita, Microsc. Res. Tech. **40**, 284 (1998).

[16] Y. Hirotsu and R. Akada, Jpn. J. Appl. Phys., Part 2 **23**, L479 (1984).
[17] T. Ohkubo, H. Kai, A. Makino, and Y. Hirotsu, Mater. Sci. Eng., A **312**, 274 (2001).
[18] T. Ohkubo and Y. Hirotsu, Phys. Rev. B **67**, 094201 (2003).
[19] M. K. Miller, *Atom Probe Tomography: Analysis at the Atomic Level* (Kluwer Academic, Dordrecht, 2000).
[20] A. Hirata and Y. Hirotsu, J. Mater. Sci. **41**, 2597 (2006).
[21] K. Kajiwara, M. Ohnuma, D. H. Ping, O. Haruyama, and K. Hono, Intermetallics **10**, 1053 (2002).
[22] D. Nagahama, T. Ohkubo, and K. Hono, Scr. Mater. **49**, 729 (2003).
[23] I. Martin, T. Ohkubo, M. Ohnuma, B. Deconihout, and K. Hono, Acta Mater. **52**, 4427 (2004).
[24] N. Tian, M. Ohnuma, T. Ohkubo, and K. Hono, Mater. Trans., JIM **46**, 2880 (2005).
[25] Y. Zhang, K. Hono, A. Inoue, A. Makino, and T. Sakurai, Acta Mater. **44**, 1497 (1996).